

# Antimodes and Graphical Anomaly Exploration via Depth Quantile Functions

Gabriel Chandler

Department of Mathematics and Statistics  
Pomona College, Claremont, CA 91711

and

Wolfgang Polonik\*

Department of Statistics  
University of California, Davis, CA 95616

E-mail: gabriel.chandler@pomona.edu and wpolonik@ucdavis.edu

January 19, 2022

## Abstract

Depth quantile functions (DQF) encode geometric information about a point cloud via functions of a single variable, whereas each observation in a data set can be associated with a single function. These functions can then be easily plotted. This is true regardless of the dimension of the data, and in fact holds for object data as well, provided a mapping to an RKHS exists. This visualization aspect proves valuable in the case of anomaly detection, where a universal definition of what constitutes an anomaly is lacking. A relationship drawn between anomalies and antimodes provides a strategy for identifying anomalous observations through visual examination of the DQF plot. The DQF in one dimension is explored, providing intuition for its behavior generally and connections to several existing methodologies are made clear. For higher dimensions and object data, the adaptive DQF is introduced and explored on several data sets with promising results.

**Keywords**— multi-scale, object data, visualization

## 1 Introduction

Anomaly detection (alternatively: outlier detection, novelty detection, etc.) can be regarded as the identification of rare observations in a data set that differ significantly from the remaining bulk of the data. There is no standard definition of an outlier or anomalous observation, though the definition provided by Hawkins (1980) captures the essence used in the current work:

*Observations which deviates so much from other observations as to arouse suspicion it was generated by a different mechanism.*

---

\*The work of W. Polonik was supported in parts by the NSF grant DMS-2015575.

Anomalous observations can be defined in terms of either density or distance. For instance, Hynman (1996) and others have defined an outlier as those lying in low density regions, while others (e.g. Burrige and Taylor, 2006, and Wilkinson, 2017) define them as observations lying far from the bulk of the data.

Considering these different points of view on outliers or anomalies, one sees that rare (anomalous) events obviously go along with low density. Furthermore, the idea of an alternative mechanism generating these observations relates to mixture distributions (albeit with low probability associated with the alternative) and thus antimodes. Certainly, deviating substantially from the bulk of the data means that the geometry, at least “locally” around the anomalous point, differs from that of non-anomalous points. Additionally, at least on a heuristic level, the midpoint between such an anomaly and a non-outlying observation is likely to live near an antimode, which should also have informative geometry. In fact, we may partially characterize an antimode as having relatively low density with an increased measure of centrality.

The aim of this paper is to show that the depth quantile function (DQF) approach put forward in Chandler and Polonik (2021) ties together these different aspects of anomalous or outlying points, particularly with respect to antimodes. In fact, we will show that aspects of the DQF provide information about both the density and the centrality of a point in the data space. Additionally, the visualization aspect that comes with the DQF approach is a great aid in identifying antimodes, and thus outliers. Due to the lack of a clear definition of what constitutes a true anomaly, a graphical summary of data, similar to the box plot in one dimension, provides the practitioner with information about unusual observations in their data that they can explore further.

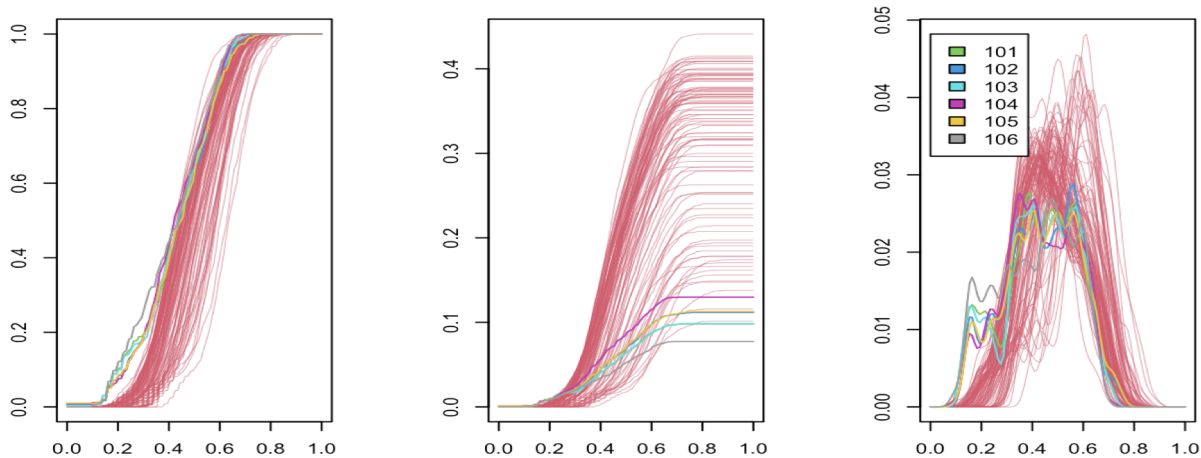


Figure 1: Functional representations via the DQF methodology for simulated data set; panels show standardized DQFs, the DQFs itself, and their 1st derivatives, respectively; Data:  $n = 100$  observations, lying in a  $d = 30$  annulus ( $r = \frac{1}{3}, R = 1$ ) centered at origin drawn from a density decreasing as a function of the norm. Data  $x_{101}, \dots, x_{105}$  form an inlying micro-cluster inside the annulus, and  $x_{106} = -x_{101}$  constitutes an isolated inlying anomaly. Anomalous observations (color-coded) show different behavior than non-anomalous observations, and micro-cluster separates itself from isolated anomaly.

It is important to note here that the visualization aspect of the DQF approach applies to any dimension and, in conjunction with the kernel trick, it can be used for non-Euclidean data as well. Indeed, as described below, the DQF maps data points, regardless of dimension, to real valued functions of a single variable, which can then be easily plotted. Figure 1 shows three representations

of these functions, which we describe in detail below, for a simulated data set that includes various notions of anomalies. This is the standard output of the R functions that accompany this work.

Other visualization approaches for high-dimensional data often don't show the flexibility displayed by the DQF. For instance, ideas like parallel coordinate plots are generally unable to aid in outlier discovery (Wilkinson, 2017). There exists an extensive literature regarding tools for detecting anomalous observations. In addition to the work above, see Hodge and Austin (2004), Aggarwal (2013) and Ruff et al. (2021) for surveys of both applications of this problem and various approaches to it. Recent work has focused on exploiting an assumed manifold structure for the non-anomalous data (e.g. Olson et al. 2018) which we discuss below.

While the DQF approach for  $d \geq 2$  has been proposed in Chandler and Polonik (2021), a detailed application to anomaly detection (including the important choice of tuning parameters) as well as the relation to antimodes was not discussed there. This connection will become particularly evident when discussing the DQF approach for  $d = 1$ , which, in turn, establishes a perhaps unexpected connection to the concept of modal intervals put forward by Lientz (1974), and the related shorth plot (Sawitzki, 1994, Einmahl et al., 2010a,b). Yet another interesting point of view to the DQF approach that has not been discussed so far is its connection to *masking*, which is a concept that goes back to Tukey (see Fisherkeller et al. 1974, Friedman and Stuetzle, 2002).

Section 2 gives an introduction to the general DQF approach in both  $d = 1$  and higher, including discussion of tuning parameters. Section 3 considers anomaly detection in  $d = 1$  and elucidates the connections to existing tools, particularly the *shorth*. Anomaly detection for  $d \geq 2$  including numerical studies on both real and simulated data is considered in Section 4. Section 5 presents a discussion of issues related to the implementation of this method and existing R code. The final section contains technical proofs.

## 2 The DQF approach

Suppose we observe data lying in  $\mathbb{R}^d$ . Chandler and Polonik (2021) introduces the DQF associated to an anchor point  $x \in \mathbb{R}^d$  as a real-valued function of a one-dimensional parameter that is generated by considering random subsets of  $\mathbb{R}^d$  containing  $x$ , and computing a measure of centrality of  $x$  within each random subset. This then results in a distribution of centralities (for each anchor point  $x$ ), and the quantile function of this distribution is the DQF corresponding to the anchor point (see below for details). The anchor point can be any point that can be covered by the random subsets considered. Below we consider two types of anchor points: data points, and midpoints between pairs of data points. The latter is not only motivated by applications to classification, as discussed in detail in Chandler and Polonik (2021), but also to alleviate challenges with notions of centrality in very high dimensions. As in Chandler and Polonik (2021), the random subsets of  $\mathbb{R}^d$  that we are using here are randomly chosen spherical cones, and the measure of centrality used here is based on Tukey's (halfspace) depth (Tukey 1975).

The essence of choosing a random subset (spherical cone) and only considering points captured inside this cone is closely related to the concept of *masking* that Tukey introduced with PRIM-9 (see Friedman and Stuetzle, 2002). The idea of masking is to display low-dimensional projections of the subset of the data points not being masked, and to then interactively change the mask and inspect the resulting changes in the display. Rather than directly visualizing projections, we compute a summary statistic of the data points selected (points not masked), namely the centrality of the anchor point within the selected data, vary the mask randomly, and display the quantile function of the summary statistic. All this is tied together by the anchor point to which the quantile function is associated to. This will be discussed further below.

## 2.1 The case $d = 1$

As said above, one of the advantages of DQF approach is to provide a methodology for the visual exploration of geometric structure in data (including outliers, clusters, etc.) in any dimension, and even for non-Euclidean data via the kernel-trick. It turns out, however, that insight can be gained by studying the one-dimensional case, which also has the benefit of providing a gentle introduction to the DQF approach.

We first introduce the so-called depth functions. For  $d = 1$ , the random subsets (cones) considered by the DQF approach are simply half-infinite intervals induced by a random split point  $S$ . Given a point  $x \in \mathbb{R}$  and a realization  $s$  of  $S$ , define

$$d_x(s) = \begin{cases} \min\{F(x), F(s) - F(x)\} & \text{if } x \leq s, \\ \min\{F(x) - F(s), 1 - F(x)\} & \text{if } x > s, \end{cases} \quad (1)$$

where we notice, for instance when  $s \geq x$ ,  $d_x(s)$  is the Tukey depth of  $x$  with respect to (the generally improper)  $F$  restricted to  $(-\infty, s]$ . Similarly,  $d_x(s)$  also is the Tukey depth of  $x$  in case  $s < x$ , but this time for  $F$  restricted to  $[s, \infty)$ . So, while the notion of centrality used by the DQF approach is Tukey's (1975) data depth (TD), it is with respect to an improper distribution, as we don't rescale the mass on the subset.

Clearly,  $d_x(s)$  is non-decreasing when  $s$  moves away from  $x$  in either direction, and the values on the boundaries ( $s = 0, 1$  if we assume the support is contained within the unit interval) are both equal to the global Tukey depth of  $x$  with respect to  $F$ , which is  $\text{TD}(x) = \min(F(x), 1 - F(x))$ . Figure 2 shows functions  $d_x(s)$  for a variety of  $x$  values on a grid with  $F$  a symmetric density comprised of two isosceles triangles.

A random split-point  $S$  now induces a distribution on the "depths" of  $x$ , and the quantile function corresponding to this distribution is then the object of interest: The DQF,  $q_x(\delta)$ , corresponding to  $x$  is now defined as the quantile function of the distribution of  $d_x(S)$ , i.e.

$$q_x(\delta) = \inf\{t \geq 0 : G(d_x(S) \leq t) \geq \delta\}, \quad (2)$$

where, for a distribution  $G$  and a measurable set  $A$ , we let  $G(A)$  denote the probability content of  $A$  under  $G$ . The parameter  $\delta$  can be thought of as measuring the scale at which information is extracted.

Empirical version are obtained by replacing  $F$  with the empirical distribution  $F_n$  based on the observations  $X_1, \dots, X_n$ , i.e.

$$\hat{q}_x(\delta) = \inf\{t \geq 0 : G(\hat{d}_x(S) \leq t | X_1, \dots, X_n) \geq \delta\},$$

where

$$\hat{d}_x(s) = \begin{cases} \min\{F_n(x), F_n(s) - F_n(x)\} & \text{if } x \leq s, \\ \min\{F_n(x) - F_n(s), 1 - F_n(x)\} & \text{if } x > s. \end{cases} \quad (3)$$

The following lemma gives some properties of the DQF that provide some important insights as discussed further below.

**Lemma 2.1.** *Let  $G$  be uniform on  $[0, 1]$  and  $F$  a continuous distribution with support contained in  $[0, 1]$ . For  $x \in [0, 1]$ , let*

$$\delta_x^* = \begin{cases} F^{-1}(2F(x)), & \text{for } F(x) \leq \frac{1}{2} \\ 1 - F^{-1}(2F(x) - 1), & \text{for } F(x) \geq \frac{1}{2}. \end{cases} \quad (4)$$



Then, for  $0 \leq \delta < \delta_x^*$ , there exists an interval  $I_{x,\delta} = [a_{x,\delta}, b_{x,\delta}] \subset [0, 1]$  of length  $\delta$  with

$$q_x(\delta) = \frac{1}{2}F(I_{x,\delta}) = F([a_{x,\delta}, x]) = F([x, b_{x,\delta}]). \quad (5)$$

Moreover, for  $\delta_x^* \leq \delta \leq 1$ , we have  $q_x(\delta) = \text{TD}(x)$ , and  $q_x(\delta) = 0$  for  $\delta \in [0, l_x]$ , where  $l_x = \sup\{b - a : x \in [a, b], F([a, b]) = 0\}$ .

REMARK: For a general continuous distribution  $G$ , a similar result holds, where the length of the interval  $I_{x,\delta}$  and the lengths of the intervals  $[a, b]$  in  $l_x$  have to be replaced by their  $G$ -measure, and  $\delta_x^*$  is replaced by  $G(\delta_x^*)$ , where here  $G$  denotes the cdf.

In words, the lemma says that for a distribution on the unit interval and a uniform distribution of split points, the DQF of a point  $x$  flattens out at its maximum value  $\text{TD}(x)$ , and the values  $q_x(\delta)$  strictly less than its maximum value equal the probability content of an interval of length  $\delta$  for which  $x$  is a *conditional median*. Being a conditional median means that the  $F$ -measure of the portion of the interval to the left of  $x$  is the same as the one of the portion to the right of  $x$  (which allows for intervals with zero  $F$ -measure, for which any point in the interval is a conditional median). We can contrast this median property with the well-known kernel density estimator, which for a box kernel, is proportional to the probability content of the interval *symmetric* about  $x$  with respect to Lebesgue measure rather than the underlying probability measure as is the case here. Another related case is the so-called shorth-plot, and this relation will be discussed in some detail below.

The last part of the lemma provides an explanation for the empirical observation that the DQF being small (almost flat) for small values of  $\delta$  is one of the important visual indicators for anchor points that correspond to an anomalous point. One of the situations in which this is of particular interest is when the anchor point  $x$  is chosen as the midpoint between two observations - see Lemma 2.2, where this case is considered in a multivariate situation.

So, it is clear that  $q_x(0) = 0$  and that  $q_x(\delta)$  has a flat part at level zero if  $x \notin \text{supp}(F)$ . As a simple corollary of Lemma 2.1, we obtain the following interesting refined result about the behavior of  $q_x(\delta)$  at  $\delta = 0$  under some additional assumptions. For  $d \geq 2$  this result can be found in Chandler and Polonik (2021), and here it directly follows from the representation of  $q_x(\delta)$  given in (5) by assuming that  $F$  is not constant in a neighborhood of  $x$ .

**Corollary 2.1.** *Suppose that  $F$  has density  $F' = f$ . Let  $x \in [0, 1]$  be such that, for some  $\epsilon > 0$ ,  $f(u) > 0$  for  $u \in [x - \epsilon, x + \epsilon]$ . Then*

$$\lim_{\delta \rightarrow 0} \frac{2q_x(\delta)}{\delta} = f(x).$$

From Lemma 2.1 and Corollary 2.1, we see that the DQF is informative at both large and small scales, i.e. for large and small values of  $\delta$ , motivating the usefulness of the entire function in examining a data set. This is in contrast to other multi-scale methods, such as the mode tree (Minnotte, 1993), which transitions from  $n$  modes to 1 (thus no information on either extreme), or a multi-scale version of the shorth which we discuss and explore below.

## 2.2 The case $d > 1$

As localization is an important aspect of the DQF for small values of  $\delta$ , one finds that half-spaces as our random subsets will not suffice. Rather, we consider subsets of the data space formed by cones, which we note that for  $d = 2$  and an opening angle of  $\alpha = \pi/4$  (the angle between a point on

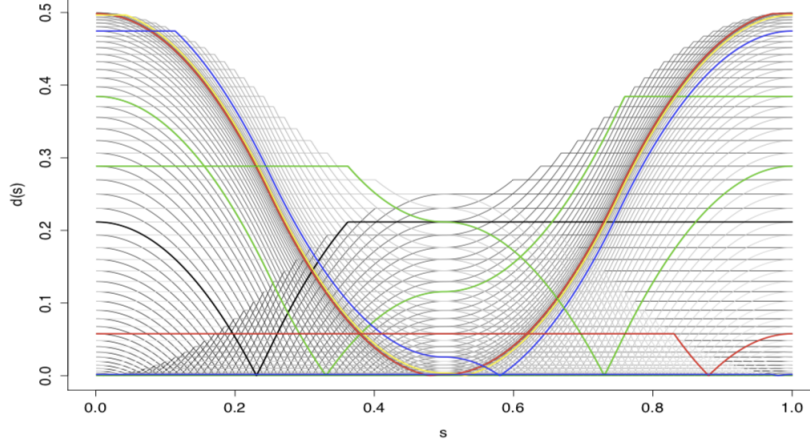


Figure 2: The function  $d_x(s)$  for a grid of  $x$  values, based on a symmetric density comprised of two isosceles triangle. The associated  $x$  value for each curve is the point at which  $d_x(s) = 0$ . Colored lines added to select points to aid visualization.

the surface of the cone and the axis of symmetry with the cone tip as the origin), are the Cartesian product of our sets in one dimension. We do not however require these sets to be aligned with our original axes. Similarly, in higher dimensions, we use spherical cones to not privilege any particular direction in our space beyond the specified axis of symmetry for the cone. The question is then how to put a distribution over cones in order to compute quantile functions.

First we discuss the construction of the empirical version of the DQF. For any two points in the data set, say  $x_i$  and  $x_j$ , let  $\ell_{ij}$  denote the line passing through them, and consider spherically symmetric cones  $C_{ij}(s)$  with  $\ell_{ij}$  as axis of symmetry,  $s$  as the tip located on  $\ell_{ij}$ , and a fixed opening angle  $\alpha$ , which is a tuning parameter. Select a point on that line as the “anchor point”  $m_{ij}$ . The choice of  $m_{ij}$  might depend on the specific application considered. In our applications, we often choose this as the midpoint,  $m_{ij} = \frac{x_i + x_j}{2}$ , but it could also be  $x_i$ , or  $x_j$ , for instance, which is what we are using in the one-dimensional case discussed above. The orientation of the cone  $C_{ij}(s)$  is such that  $m_{ij}$  is contained inside. In other words, the orientation of the cones flips depending on which side of  $m_{ij}$  the tip lies.

Given any such cone  $C_{ij}(s)$ , split the cone into two parts  $A_{ij}(s)$  and  $B_{ij}(s)$  with boundaries formed by the surface of the cone and the hyperplane orthogonal to  $\ell_{ij}$  passing through  $m_{ij}$ . Let  $A_{ij}(s)$  be the resulting cone, and  $B_{ij}(s)$  be the frustum. Then, the measure of centrality of  $m_{ij}$  that we are using is the depth

$$\hat{d}_{ij}(s) = \min (F_n(A_{ij}(s)), F_n(B_{ij}(s))).$$

Equivalently, one can think of constructing  $\hat{d}_{ij}(s)$  by projecting the data lying inside the cone  $C_{ij}(s)$  onto  $\ell_{ij}$ . Then  $\hat{d}_{ij}(s)$  is the one dimensional Tukey depth of  $m_{ij}$  among these projections.

Finally, we choose the tip randomly according to a distribution  $G_{i,j}(s)$  along the axis of symmetry  $\ell_{ij}$ . (We will comment below on ways to choose  $G_{i,j}$ .) The DQF  $\hat{q}_{ij}(\delta)$  is then defined as the quantile function of the distribution of the random depths with respect to  $G_{i,j}(s)$  (conditional on  $X_1, \dots, X_n$ ), i.e.

$$\hat{q}_{ij}(\delta) = \inf \{t > 0 : G_{ij}(s : \hat{d}_{ij}(s) \leq t) \geq \delta\},$$

where, for a measurable set  $D \subset \ell_{ij}$  we let  $G(D)$  denote the  $G$ -measure of  $D$ . To reduce the total number of functions to consider, different approaches might be considered. A natural approach is

to use averaging: For each data point  $x_i$ , average the functions  $\hat{q}_{ij}(\delta)$  over  $j \neq i$ , i.e. for each  $x_i$ , we consider

$$\bar{q}_i(\delta) = \frac{1}{n-1} \sum_{\substack{j=1 \\ j \neq i}}^n \hat{q}_{ij}(\delta).$$

More robust approaches include Winsorized averages, truncated averages, etc. A slightly different summary is to consider normalized averages of the DQFs of the form

$$\tilde{q}_i(\delta) = \frac{\bar{q}_i(\delta)}{\bar{q}_i(1)}.$$

These normalized averages both embed the global behavior of the DQF at all  $\delta$  values as well as focus solely on the shape of the DQF.

POPULATION VERSIONS of the empirical depth functions  $\hat{d}_{ij}(s)$  and the corresponding empirical DQFs are defined as follows. For  $x, y \in \mathbb{R}^d$ , let  $\ell_{x,y}$  denote the line passing through both  $x$  and  $y$ . For  $s \in \ell_{x,y}$  let  $C_{x,y}(s)$  denote the spherically symmetric cone in  $\mathbb{R}^d$  with tip  $s$  containing the anchor point, say  $m_{x,y} = \frac{x+y}{2}$ , with axis of symmetry given by  $\ell_{x,y}$ , and with opening angle given by the tuning parameter  $\alpha$ . The hyperplane through  $m_{x,y}$  perpendicular to  $u$  then divides  $C_{x,y}(s)$  into two sets, a cone  $A_{x,y}(s)$  and a frustum  $B_{x,y}(s)$ , where for definiteness, the intersection of the hyperplane and the cone (the base of  $A_{x,y}(s)$  or the top of  $B_{x,y}(s)$ ) is considered to be part of  $A_{x,y}(s)$  but not of  $B_{x,y}(s)$ . Then,

$$d_{x,y}(s) = \min(F(A_{x,y}), F(B_{x,y})).$$

Similar to the empirical version,  $d_{x,y}(s)$  is the one-dimensional Tukey depth of the (sub)distribution obtained by projecting the mass of the cone  $C_{x,y}(s)$  onto the axis of symmetry  $\ell_{x,y}$ . Figure 3 illustrates this for a two-dimensional bi-modal density.

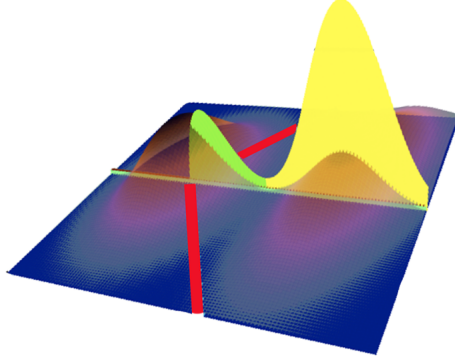


Figure 3: A 2-dimensional bimodal distribution (blue to purple), a given anchor point  $m_{x,y}$  (green/yellow region intersection), direction  $\ell_{x,y}$  (green line in plane), and cone tip  $s$  (convergence of red cone boundaries). Green/yellow function over  $\ell_{x,y}$  indicates the probability mass inside the cone projected onto  $\ell_{x,y}$ . For this cone tip,  $d_{x,y}(s)$  would equal the green area under the one-dimensional curve rather than the larger yellow area.

Again, choosing the tip randomly on the line  $\ell_{x,y}$  according to  $S \sim G = G_{x,y}$  results in a random variable  $d_{x,y}(S)$  whose quantile function is the DQF  $q_{x,y}(\delta)$ . Formally,

$$q_{x,y}(\delta) = \inf\{t > 0 : G_{x,y}(d_{x,y}(S) \leq t) \geq t\}.$$

The empirical average  $\bar{q}_i(\delta)$  corresponds to

$$\bar{q}_x(\delta) = \mathbb{E}[q_{x,Y}(\delta)], \quad Y \sim F,$$

and similarly  $\tilde{q}_x(\delta) = \frac{\bar{q}_x(\delta)}{\bar{q}_x(1)}$  is the normalized expected DQF. As already mentioned, a result for  $d \geq 2$ , analogous to Corollary 2.1 can be found in Chandler and Polonik (2021). The flatness of the DQF for anchor points lying outside the support of  $F$ , i.e. a result analogous to the last assertion of Lemma 2.1, also holds for  $d \geq 2$ , as shown in the following result.

We use the following setting: For a given distribution  $F$  on  $\mathbb{R}^d$  and  $x, y \in \mathbb{R}^d$ , let  $[a_{x,y}, b_{x,y}] \subseteq \ell_{x,y}$  denote the range of the push-forward distribution on  $\ell_{x,y}$  obtained by the projection map  $\pi_{x,y}(z)$ , which is the orthogonal projection of  $z \in \mathbb{R}^d$  onto  $\ell_{x,y}$ . We assume  $\|b_{x,y} - a_{x,y}\| > 0$ . Let  $U[a_{x,y}, b_{x,y}]$  denote the uniform distribution on the range  $[a_{x,y}, b_{x,y}]$ . This is a one-dimensional distribution on an interval of length  $\|b_{x,y} - a_{x,y}\|$ . Also, we represent  $\ell_{x,y}$  as  $\ell_{x,y} = \{z \in \mathbb{R}^d : z = m_{x,y} + su_{x,y}, s \in \mathbb{R}\}$ , where  $m_{x,y}$  is the anchor point, and  $u_{x,y} \in S^{d-1}$  is the unit vector giving the direction of  $\ell_{x,y}$ .

**Lemma 2.2.** *In the above setting, for given  $x, y \in \mathbb{R}$  let  $G_{x,y} = U[a_{x,y}, b_{x,y}]$ . Let*

$$t_{x,y}^\pm = \inf_{t \geq 0} \{s = m_{x,y} \pm tu_{x,y}, s \in [a_{x,y}, b_{x,y}] \text{ and } F(A_{x,y}(s)) \neq 0\}.$$

Then,

$$q_{x,y}(\delta) = 0 \quad \text{for } \delta \in [0, \delta_{x,y}],$$

where  $\delta_{x,y} = \frac{t_{x,y}^+ + t_{x,y}^-}{\|b_{x,y} - a_{x,y}\|} = G_{x,y}([s_{x,y}^-, s_{x,y}^+])$ , where  $s_{x,y}^\pm = m_{x,y} \pm t_{x,y}^\pm u$ .

Geometrically, the quantity  $t_{x,y}^+ + t_{x,y}^- = \|s_{x,y}^+ - s_{x,y}^-\|$  is the sum of the heights of two cones  $A_{x,y}(s_{x,y}^+), A_{x,y}(s_{x,y}^-)$ . Note that the two cones point in opposite directions, and by definition of  $t_{x,y}^+$  and  $t_{x,y}^-$ , they are chosen such that they give the largest spherically symmetric cones under consideration that do not intersect with the support of  $F$ . Also note that the two cones belong to the same anchor point that is lying at the center of the bases of these two cones. So suppose that the support of  $F$  has a hole and the anchor point  $m_{x,y}$  lies in this hole (think of  $m_{x,y}$  as the midpoint between  $x$  and  $y$ ), then the  $G_{x,y}$ -measure of the combined heights,  $G_{x,y}([s_{x,y}^-, s_{x,y}^+])$ , measures some aspects of the geometry of the hole.

Moreover, if, for a given  $x$ , there is a high probability that a randomly chosen  $y$  is such that the corresponding anchor point lies off the support of  $F$ , then  $\bar{q}_x(\delta)$  will also be small for a range of small values of  $\delta$ . (Recall also that everything depends on the opening angle of the cones as well.)

Also note that Lemma 2.2 is a generalization of the one-dimensional case presented in the last part of Lemma 2.1. In this one-dimensional case there is of course no need to consider pairs since there is only one axis. For further discussion of the population version and theoretical properties of the corresponding estimators, see Chandler and Polonik (2021).

### 2.2.1 Choice of $G_{x,y}$ - The Adaptive DQF

The function  $G_{x,y}$  is one of the “tuning parameters” of the DQF approach. Here we discuss some possible choices and their motivation. This discussion will similarly hold true for the empirical analog,  $G_{i,j}$ .

*Uniform distributions.* In the setting of Lemma 2.2 above,  $G_{x,y}$  was chosen as the uniform distribution on  $\ell_{x,y}$  over a certain range  $[a_{x,y}, b_{x,y}]$ . The actual choice of this range might depend on  $x, y$ , or not. We discuss some of the choices here.

(i) One choice for  $[a_{x,y}, b_{x,y}]$  is given by the range of the push-forward distribution under the projection of  $F$  onto  $\ell_{x,y}$ . In practice, we of course use the empirical analog (projecting the empirical distribution onto  $\ell_{x,y}$ ). One of the motivations for this adaptive choice is as follows:

Suppose our underlying distribution on  $\mathbb{R}^d$  is of the form  $(1 - \epsilon)U(C) + \epsilon Q$ , where  $\epsilon > 0$  is “small”,  $U(C)$  is a uniform distribution on a set  $C$ , and  $\text{supp}(Q) \cap C = \emptyset$ . The distribution  $Q$  models anomalies. Suppose we use  $\frac{x+y}{2}$  as anchor point. For  $X \sim U(C)$  and  $y \in \text{supp}(Q)$ , the gap between  $C$  and  $y$  is measured by the distribution of  $\delta_{X,y}$ , the length of the zero-interval of  $q_{X,y}$  from Lemma 2.2. Notice, however, that the same physical gap (Hausdorff distance between  $\text{supp}(Q)$  and  $C$ ) can lead to different distributions of  $\delta_{X,y}$ , depending on where  $Q$  is located. This is because of the adaptive choice of  $G_{x,y}$ . For instance, suppose that  $C$  is an elongated ellipsoid, and  $\text{supp}(Q)$  is a ball with Hausdorff distance to  $C$  being a given value. Then, we can see from Lemma 2.2, that with this adaptive choice of  $G_{x,y}$ , the values of  $\delta_{x,y}$  will tend to be smaller if  $Q$  is located along the main axis of  $C$  than if it is located along one of the minor axis. (The reason is that the range of the corresponding push-forward distributions tends to be larger in the former case, and  $\delta_{X,y}$  is the physical length of the gap divided by the range.) This, in turn, will lead to smaller values of the averaged DQF,  $\bar{q}_y(\delta)$ ,  $y \in Q$  for small values of  $\delta$ . The rationale for this adaptive choice is similar to that of a Mahalanobis distance, as a point a fixed distance from  $C$  in the direction of a minor axis is arguably more of an anomaly than one along the main axis. Of course the same rationale holds if we have a non-uniform distribution on  $C$ .

(ii) A variation of the just discussed choice of  $G_{x,y}$  is to still use a uniform distribution on  $\ell_{x,y}$ , but instead of using the range of the projections as the support of  $G_{x,y}$ , we choose the uniform with the same center, but with length being a constant times a robust measure of spread of the projections, such as a Winsorized standard deviation, or an inter-quartile range. For motivation, consider data living on a plane with an anomalous observation  $x$  living off of it, and suppose that  $y$  is such that  $\ell_{x,y}$  is orthogonal to the plane. By using a robust measure of spread,  $\delta_{x,y}$  is effectively 1 as  $G$  will be degenerate.

(iii) A third choice of uniform type distributions for  $G_{x,y}$  is to choose the same uniform distribution for all pairs  $(x, y)$  (of course this assumes that the support of  $F$  is compact). The motivation for choosing  $G_{x,y}$  independent of  $x, y$  is given by the fact that if  $f(x^*) > 0$ , where  $x^*$  denotes the anchor point, then the slope of  $q_{x,y}(\delta)$  at 0 is proportional to  $f(x^*)$  (see Chandler and Polonik, 2021, Lemma 2.2(c)). This non-adaptive choice for  $G_{x,y}$  is used throughout Chandler and Polonik (2021). However, the emphasis in the current context of anomaly detection is a flat behavior for small values of  $\delta$ . It is thus not too surprising that this choice of  $G_{x,y}$  is typically outperformed by other choices, dubbed the “adaptive DQF” (aDQF), as seen in the numerical studies. It is clear that a good choice of  $G_{x,y}$  depends on the goal.

*Normal distribution:* A choice for  $G_{x,y}$  showing a strong performance in our simulation studies is a normal distribution on  $\ell_{x,y}$  with mean  $m_{x,y}$  and variance equal to the variance (or a robust version of it) of the push-forward distribution of the projection of  $F$  onto  $\ell_{x,y}$ . This choice is motivated by a preferred choice of the tip close to  $m_{x,y}$ , which leads to a more pronounced zero-interval, meaning that  $\delta_{x,y}$  (see Lemma 2.2) tends to be longer, leading to a visual enhancement of anomalies in the DQF plots. Of course other choice might be possible, including distributions with heavier tails such as  $t$ -distributions, etc. For non-adaptive  $G_{x,y}$ , changing the base distribution amounts simply to a non-linear rescaling of the horizontal axis in the DQF plot, and accordingly was not considered in Chandler and Polonik (2021).

### 2.2.2 Choice of the opening angle $\alpha$

Similar to the distribution  $G_{x,y}(\delta)$ , the choice of the opening angle of the cones of course influences the shape of the DQFs, and a good choice will depend on the underlying geometry and of course also on the dimension. As for the dimension, for a spherical cone in  $\mathbb{R}^d$  with a given height  $h$  and radius of the base  $r$ , it is straightforward to see that in order for the volume of this cone not to

tend to zero as  $d \rightarrow \infty$ , one needs  $r = O(\sqrt{d})$ . This knowledge is of limited use, however, as, for instance, the data often lies on a lower dimensional manifold. For practical application everything will depend on the constant  $c$  when choosing  $r = c\sqrt{d}$ , and again a good choice of  $c$  will depend on the underlying geometry.

Now, while a certain robustness to the choice of  $\alpha$  has been observed in our numerical studies, a more refined study of the DQF plots indicates subtle, but (at least visually) important differences for different angles. Our recommendation here is to consider a few choices of  $\alpha$  at once and to compare the resulting plots. Computationally, this does not pose a huge burden, because in order to determine whether a point  $w$  falls inside a cone with tip  $s$  and axis of symmetry  $\ell_{x,y}$ , all we need to determine is the angle between  $\ell_{x,y}$  and  $\overline{sw}$ . Then one simply compares this angle to the opening angle.

### 3 A connection to the shorth in the case $d=1$

For anomalies of the type that are far from the bulk of the data, techniques such as the box plot are both well-known and effective. Instead, we consider the density based definition of an anomaly for  $d=1$ . We look at the case where anomalous observations exist in particular types of antimodes, which we call “holes”, characterized by a low density region surrounded closely by much higher density regions. Such observations are occasionally referred to as “inliers” in the literature (for example, Talagala et al, 2021).

We consider the distribution used in Einmahl et al. (2010a), visualized in Figure 4 and defined as:

$$f_X(x) = \begin{cases} 0.05 & \text{for } |x| \leq 0.13 \\ 0.987[\phi(x) + \phi(|x| - 0.13)] & \text{for } 0.13 < |x| < 0.26 \\ 0.987\phi(x) & \text{for } |x| \geq 0.26. \end{cases} \quad (6)$$

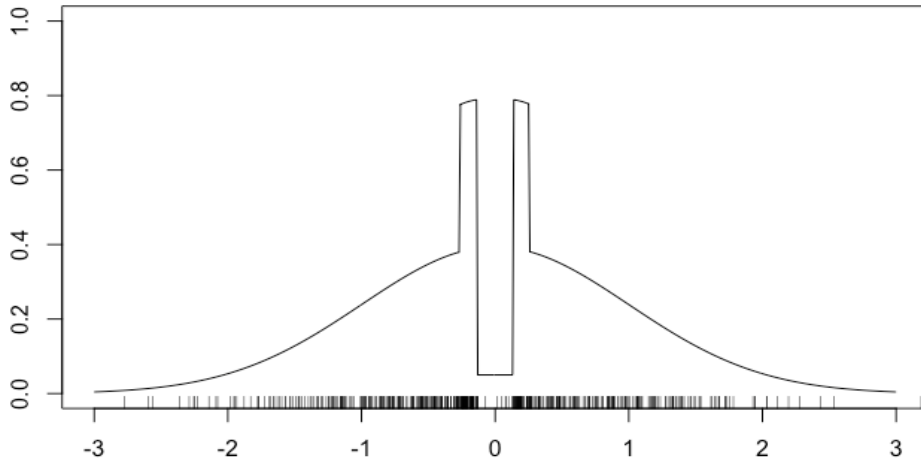


Figure 4: The density  $f$  defined in (6) with a rug plot of a random sample of size  $n = 500$ .

Einmahl et al. (2010a) motivated the *shorth plot* in part by demonstrating the shortcomings of standard techniques like the histogram or kernel density estimation in distinguishing this density (and its antimode) from a standard normal density based on a random sample. Just as the DQF

$q_x(\delta)$  is related to the probability measure of an interval of size  $\delta$  for which  $x$  is the “median”, the shorth,  $S_\alpha(x)$ , also relates the length of a particular interval with its probability content, specifically

$$S_\alpha(x) = \inf\{|I| : P(I) \geq \alpha, I \in \mathcal{I}_x\},$$

where  $\mathcal{I}_x$  is the class of intervals containing the point  $x$ . A similar approach was considered by Lientz (1974), where the set  $\mathcal{I}_x$  was the set of intervals with *midpoint*  $x$ . Empirical versions are found by again replacing the probability measure with its empirical counterpart.

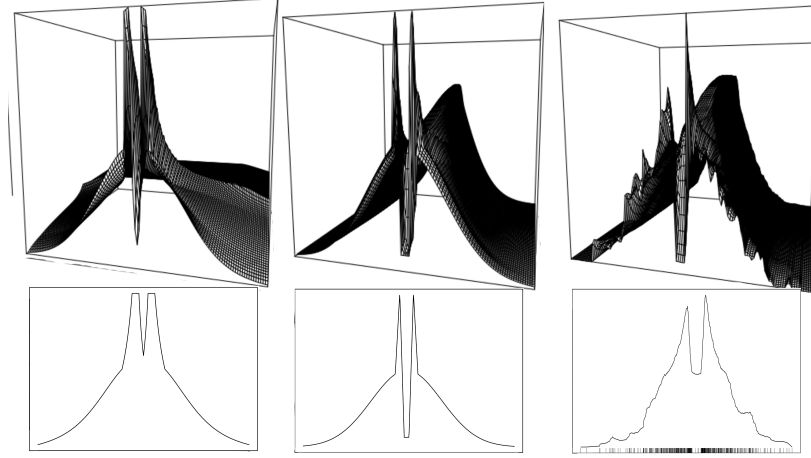


Figure 5: (left) reciprocal of the shorth over all  $\alpha$ ; (middle) DQF over all  $\delta$ ; (right) estimated DQF based on a sample of size  $n = 500$ , smoothed over  $\delta$ . All have been scaled at each  $\alpha(\delta)$  to aid in visualization. Bottom shows individual slices at individual values of the scale parameter.

The shorth-plot was introduced as a function in  $x$  for a given parameter  $\alpha$  in Sawitzki (1994). The shorth-process considered in Einmahl et al. (2010b) is studied as a process in both  $x$  and  $\alpha$ . The DQF is defined as a function in the parameter  $\delta$  for each fixed  $x$ , but of course for  $d = 1$ , it can also be plotted as a function in  $x$ . Figure 5 provides plots of these functions in both  $x$  and the corresponding parameter. To make them comparable, we plot the reciprocal of  $S_\alpha(x)$  (left figure), in addition to normalizing each plot such that, for a fixed value of the scale parameter, the integral over  $x$  is 1. This means that for small parameter values, both functions (in  $x$ ) might be considered as some type of density estimator. However, neither of these approaches is to be understood as such. Indeed, particularly in high dimensions when the curse of dimensionality kicks in, we are aiming at extracting more structural information in the sense of feature extraction.

One notable feature is that, in the low density “hole”, the shorth is “v”-shaped, while the DQF (both population and smoothed empirical versions) is flat, matching the underlying density. To see why this is, consider the point  $x = 0.10$ , which exists in the “hole”, though near its right hand boundary of 0.13. The interval of length 0.15 for the DQF will be approximately  $(-0.015, 0.135)$ , almost entirely in the “hole,” and something similar will be true for any  $x$  value in the “hole.” Meanwhile, the interval of the same length that will be considered by the shorth will be  $(0.1, .25)$  (corresponding to  $\alpha=0.095$ ). Thus, as  $x$  nears the boundary of the “hole,” the intervals instead increasingly resemble the intervals of non-anomalous points, masking the hole and resulting in the observed “v” shape.

A second feature of figure 5 is that, for large  $\alpha$ , the information quality tends to degrade as  $\alpha \rightarrow 1$ , since  $S_1(x) = |\text{supp}(F)|$  for all  $x$ . This is in contrast to the DQF, which, by Lemma 2.1 yields information about the centrality of  $x$  for large  $\delta$ . Thus, we consider visualization of the entire

function for every point in the data set, as seen in figure 6. Whereas the visualization presented in figure 5 will not be possible in other dimensions, plotting the function for each data point will be. Note the increased variability, especially for small quantiles, in the bimodal case.

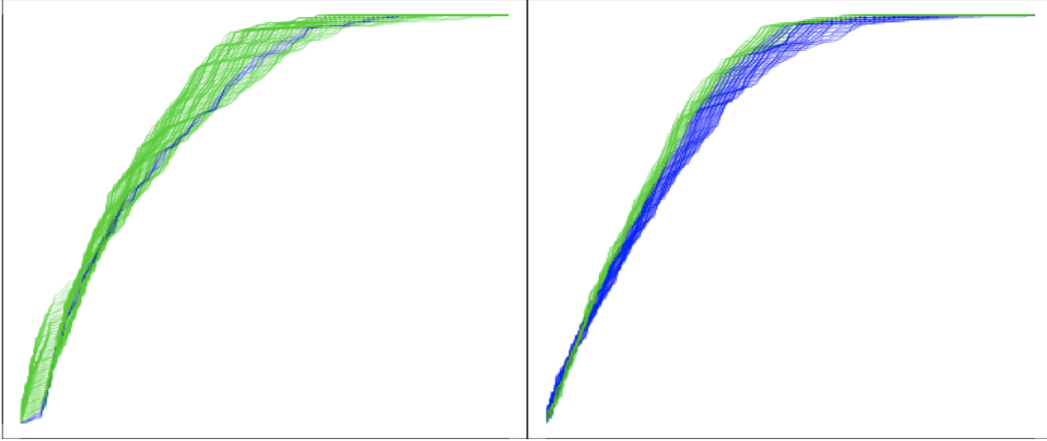


Figure 6: The (normalized) DQFs ( $\tilde{q}_i(\delta)$ ) for both a random sample of size  $n = 500$  from density (6) (left) and a standard normal density (right). Only points with  $|x| < .26$  are shown for visualization purposes. Points for which  $|x| < .13$  correspond to blue lines.

## 4 Anomaly detection for $d \geq 2$ and object data

In this section numerical studies of the DQF approach to anomaly detection are presented and discussed. We fix the cone angle  $\alpha = \pi/4$  unless mentioned otherwise. We also drop the axis from the plots of the DQFs and their derivatives, because the scale is not of importance for our discussion. Recall that as described in subsection 2.2.1 (see Uniform distribution (iii)), the non-adaptive DQF uses the same (uniform) distribution  $G_{ij}$  for all  $i, j$ .

### 4.1 Anomaly detection in $d = 2$

As in the case of  $d = 1$ , two-dimensional data is again easily visualizable, allowing identification of data points lying far from the center of the point cloud to be done via a simple scatter plot. Thus, we again consider the case of outliers living in “holes” in the center of the point cloud, and use the observations themselves as the anchor points ( $m_{ij} = x_i$ ). To this end, we use a 2-dimensional version of the density in (6) by rotating it about the  $y$ -axis. Namely, we let  $R \sim f$  and  $\theta \sim U(0, 2\pi)$ , and have  $X = R \cos(\theta)$  and  $Y = R \sin(\theta)$ . Figure 7 compares the DQF at  $\delta = 0.08$  to a kernel density estimate for a sample size of  $n = 400$ , and compares DQFs corresponding to observations inside and outside the “hole”. As for the comparison to the kernel estimate, recall that the multivariate version of Corollary 2.1 (see Chandler and Polonik, 2021) indicates that up to a scaling factor,  $\tilde{q}_i(\delta)$ , for small values of  $\delta$ , is determined by the value of the underlying density at the anchor point. Unlike the kernel smoothed estimate, there is strong visual evidence that there is a low density region within the high density region. By considering the full DQFs corresponding to each observation, we see that discriminating information is contained in multiple ranges of  $\delta$ .



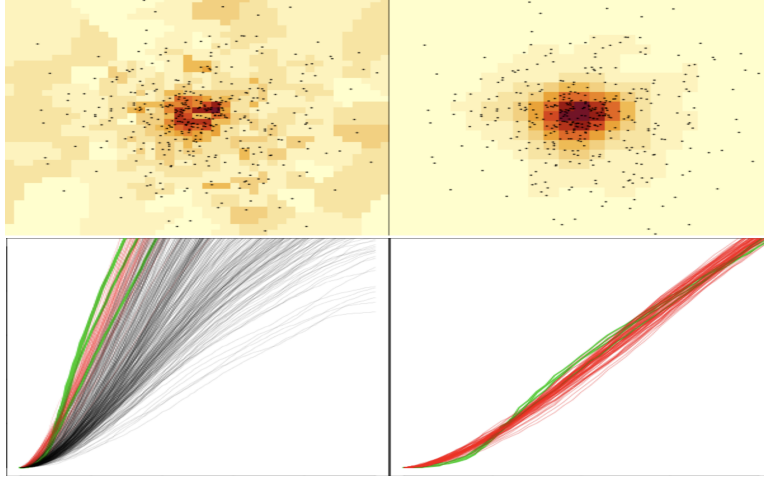


Figure 7: Piece-wise constant function based on  $\bar{q}_i(0.08)$  (top left) vs kernel density estimate with normal reference bandwidth (top right), based on sample of size  $n = 400$  from 2-dim. (rotationally symmetric) version of density (6). Portions of averaged DQF  $\bar{q}_i(\delta)$  (bottom left) and normalized version  $\tilde{q}_i(\delta)$  (bottom right) for data points. Green corresponds to points such that  $\|x\| \leq .13$  (inside hole) while red correspond to points such that  $.13 < \|x\| \leq .26$ . Functions corresponding to non-central points not plotted in bottom right plot for visualization purposes.

## 4.2 Anomaly detection in $d > 2$

As the dimension of the data increases, issues related to the curse of dimensionality arise. A particularly salient one for the current method is that the fraction of points living on the boundary of the convex hull increases in dimension (Rényi and Sulanke, 1963). Points living on this boundary will tend to have very small half space depth. As half space depth underlies the construction of the depth quantile functions, in high dimensions the DQF for a large quantity of points will have nearly identical behavior, which empirically has been seen to be constant functions at 0 (or  $1/n$  depending on how the observation in question is handled). Thus, the ability to recognize anomalous observations is hampered. This provides an additional rational for using  $m_{ij} = \frac{x_i + x_j}{2}$  as our anchor points. Beyond having the aforementioned benefit of relating to antimodes for anomalous observations, these points are very likely to live in the interior of the convex hull and thus return informative (a)DQFs. Each observation is then associated with the averaged (a)DQF over midpoints formed between itself and other observations. Considering midpoints has the additional benefit of somewhat reducing the computational complexity of the algorithm, from  $n(n - 1)$  comparisons when the observations themselves are the “anchor points” to  $\binom{n}{2}$  when using midpoints. In the applications that follow, the averaged (a)DQFs are based on a random sample of 40 pairs rather than all pairs of points, further reducing the computational burden of the method.

A common feature of high dimensional data is the so-called manifold hypothesis (Fefferman et al. 2016) that posits that the data often lives (at least approximately) on a manifold of much lower dimension than the  $d$ -dimensional ambient space. This fact is often exploited by dimension reduction algorithms, either linear (for instance, principal component analysis) or non-linear (for instance, Isomap by Tenenbaum, et al. 2000). Certainly an observation far in the tails of the point cloud might be considered anomalous, and this is the higher dimensional analog of what the box plot is designed to detect. Considering a definition of an outlier as an observation that is generated according to a different mechanism from the rest of the data set, such a point may lie off of the

manifold, despite otherwise living “near” the point cloud (with respect to the ambient space).

A particular benefit of the DQF approach is adaptivity to sparsity. Suppose that the non-anomalous data lives in a  $d'$  dimensional subspace of the ambient space with dimension  $d$ ,  $d' < d$ . For any two non-anomalous points, the line  $\ell_{ij}$  will also live in this subspace, and the intersection of our  $d$ -dimensional cones with this subspace will be cones of dimension  $d'$ . In other words, the DQF approach will behave as if we had done appropriate dimension reduction beforehand.

In the following empirical studies, we use midpoints as anchor points, i.e.  $m_{ij} = \frac{x_i + x_j}{2}$ . The aDQF uses a normal base distribution, centered at  $m_{ij}$  with variance proportional to the  $(\frac{n-6}{n})100\%$ -Windsorized variance of the projected (onto  $\ell_{ij}$ ) data. In the Euclidean case, the data is first  $z$ -scaled.

#### 4.2.1 Simulation Study

Consider the following example: 100 observations live on a 2-manifold defined by  $y_3 = 2 \cos((y_1 - .5)\pi)$  with  $(y_1, y_2)$  uniform in the unit square. A single observation lives at the point  $(0.5, 0.5, 1.5)$ , so that the manifold is curving around this observation. This point cloud is then embedded in  $d = 30$  via a randomly generated linear transformation to form the data set we consider. Figure 8 shows the manifold in 3 space before mapping to the higher dimensional space, as well as the corresponding normalized aDQFs  $\tilde{q}_i(\delta)$ 's. The function corresponding to the outlying observation differentiates itself from the bulk of the data, including but not limited to a long zero interval. Considering the zero interval of the (a)DQFs means to look for “large distance gaps,” measured by  $\delta_{x,y}$  (see Lemma 2.2). To explore the sense in which the DQF approach to measuring distance gaps can facilitate anomaly detection, we contrast the DQF approach to *stray* (Talagala et al, 2021), an extension of the *HDoutliers* algorithm (Wilkinson, 2017), a well-studied and popular anomaly detection method based on the distribution of the  $k$ -nearest neighbors distances. For this data set, the *stray* algorithm ranks the true outlier as the 3<sup>rd</sup> most unusual point out of 101 (using oracle value of tuning parameter of  $k = 1$ ). The most outlying point according to *stray* corresponds to the function that is the smallest for intermediate values of  $\delta$  in the figure.

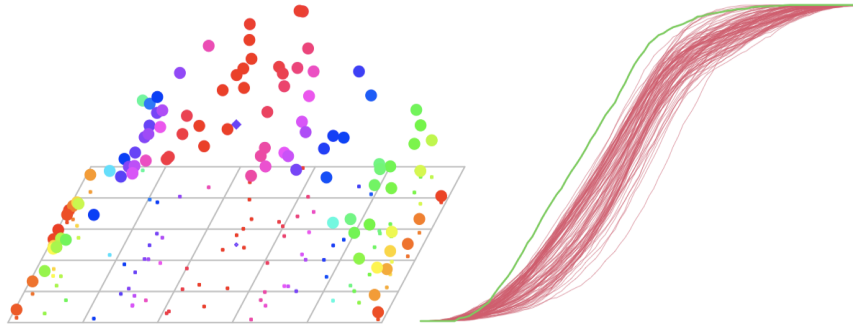


Figure 8:  $n = 100$  living on a 2-manifold embedded in  $d = 30$  with  $x_{101}$  living off the manifold. (left) Data before mapping to ambient space, color coded by vertical height, outlier as diamond, with rug plot (right) Normalized aDQFs  $\tilde{q}_i(\delta)$  with outlier in green.

As a more rigorous comparison, we simulated from several different models for high dimensional data with a single anomaly added to the point cloud. Our evaluation criterion is the rank of the true outlier according to the three methods. The rank of the outlier for the (a)DQFs corresponds

$D$	$d$	$n$	DQF	aDQF	stray
50	2	80	0.994 (1.01)	0.998 (1.00)	0.60 (1.79)
100	6 + noise	100	0.39 (3.49)	0.91 (1.12)	0.22 (4.2)
30	2 (non-linear)	101	0.93 (1.22)	0.97 (1.07)	0.67 (1.50)
30	30	50	0.54 (2.76)	0.54 (2.80)	0.20 (8.82)

Table 1: Simulation results comparing DQF, aDQF and *stray* for  $d$  dimensional data embedded in a  $D$  dimensional ambient space. One outlier present in all cases. Results are proportion of simulations where outlier is identified as most outlying observation (average rank of true outlier).

DQF \ Stray	Correct	Incorrect
	Correct	Incorrect
Correct	932	42
Incorrect	23	3

Table 2: Simulation results for a noisy version of the non-linear manifold example. Outlier is  $x_{101} = (0.5, 0.5, 0) + MVN(0, .05^2 I)$ .

to the rank at the smallest  $\delta$  such that  $\arg \min_i \bar{q}_i(\delta)$  is unique. Doing this ignores the multi-scale nature of the method. Indeed, we have seen in Figures 1 and 8, the most compelling information may be for  $\delta$  away from 0, and in the case of anomalous micro-clusters as seen in Figure 1, the distance gap is actually smallest for the anomalous observations. However, in this study we explore isolated anomalies and thus rely on Lemma 2.2 and use small values of  $\delta$ . For *stray*, rank is based on the value of the outlier score, optimized over the parameter  $k$ . Table 1 contains results for the simulation set-ups, which we describe here.

The first model generates  $(Y_1, Y_2) \sim U(0, 1)^2$ . A sample size of  $n = 80$  is then embedded in  $D = 50$  space via a random linear map with matrix coefficients chosen uniformly on  $(-1, 1)$ . A single observation is modified by adding a vector orthogonal to the plane with norm 0.4, that now constitutes the outlier. (Both the observation and the orthogonal vector are selected randomly.) The second simulation generates  $n = 100$  points uniformly in the 6-dimensional unit hyper-cube before embedding it into an ambient space of  $D = 100$  in the same manner as above. Noise is then added of the form  $\epsilon \sim MVN(0, .05^2 I)$ . The outlier is again generated by adding a vector, orthogonal to the 6 dimensional hyperplane, now with norm 10, to a single observation. The third simulation generates 100 points on the non-linear manifold described above, with a 101<sup>st</sup> at  $(.5, .5, 1)$  prior to being mapped into the ambient space of  $D = 30$ . Finally, we compare the two methods outside of a manifold structure. To this end,  $n = 50$  multivariate standard normal draws are taken in  $D = 30$ . To obtain an outlier, the first component is set to 6 for a single observation.

In all cases, the aDQF outperforms the ranks provided by *stray* according to both metrics considered. Furthermore, the aDQF outperforms the non-adaptive version in all simulations where the manifold hypothesis held true. Interestingly, in a similar simulation to the 3<sup>rd</sup> one above, it was very uncommon for a given data set to confuse both methods, suggesting that the information used in the DQF is quite different to the distances used by *stray*, see table 2. Finally, improved results were observed for the aDQF using a normal base distribution  $G_{ij}$  vs a uniform. For instance, in the 6 dimensional subspace example, a uniform  $G_{ij}$  with support proportional to the Windsorized standard deviation identified the outlier correctly only 46% of the time.

### 4.2.2 Real Data

As a real data example, we consider the *multiple features* data set available at the UCI Machine Learning Repository (<https://archive.ics.uci.edu/>). The data set consists of  $d=649$  features of handwritten digits, with 200 observations for each digit. This data set was considered in Chandler and Polonik (2021), where a data set consisting of all “6” and “9” observations were contaminated with 20 “0”s. Figure 9 considers all 200 “4” digits and the first 5 “5” digits in the data set. The DQFs again use midpoints as anchor points. The 5 anomalous observations clearly separate themselves out from the rest of the data, whereas *stray* assigns ranks 2,3,4,10 and 11 to them. Curiously, the visual information in the non-adaptive DQF here is better than the aDQF, likely a function of the shape of the manifold.

Next, we consider a data set of size  $n = 210$ , consisting of all “5” observations and the first 10 “9” observations. Based on the visually chosen 0.42 quantile, the area under the response operator curve (ROC AUC) is 0.97 (0.989 if based on the normalized DQF), compared to 0.915 for *stray*. Comparing all 200 “6” observations to the second 10 “9” observations yielded an AUC of 0.975 versus 0.95 for *stray*.

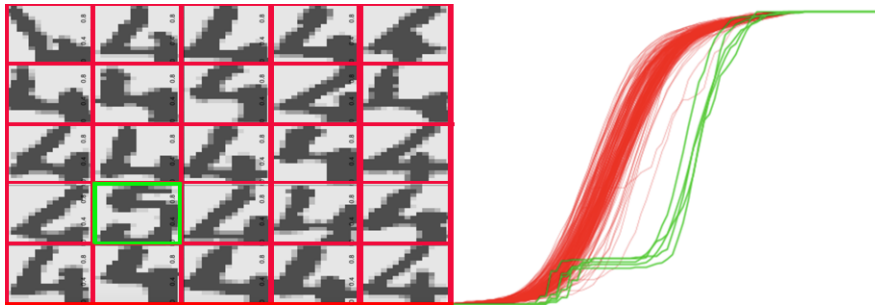


Figure 9: Normalized DQFs  $\tilde{q}_i(\delta)$  from the *multiple features* data set. 200 “4” digits (red) and the first 5 “5” digits (green).

### 4.3 Object Data - Kernelized DQF

Given that the (a)DQF only requires computing distances between observations, any object data for which a kernel function is defined can be visualized by using the corresponding RKHS geometry via the (a)DQF. Here we consider two such examples.

The first one is the shape classification task studied in Reininghaus et al. (2015), where we analyze 21 surface meshes of bodies in different poses, in particular the first 21 observations of the SHREC 2014 synthetic data set. The first 20 correspond to one body, while the 21<sup>st</sup> corresponds to a different body, which we regard as an outlier.

The approach to compare these surface meshes consists of various steps that we now briefly indicate. The first step is to construct the so-called Heat Kernel Signature (HKS) for each of the surface meshes. The HKS is a function of the (eigenvalues and eigenvectors) of the estimated Laplace-Beltrami operator (see Sun et al., 2009). One can think of the HKS as a piece-wise linear function on the surface mesh, whose values somehow reflect geometric aspects of the surface. Comparing these functions directly is not possible, because they live on different surfaces. Thus, certain features of these functions are extracted. This is accomplished by constructing a persistence diagram for each of the HKSs, using their (lower) level set filtration. We refer to Chazal and Michel (2021) or Wasserman (2018) for introductions to persistent homology, including persistence

diagrams. In a nutshell, these persistence diagrams measure the number of topological features of the level sets of the HKSs along with their significance (persistence), which in turn is related to the heights of the critical points of the functions. In particular, it is not a single level set that is considered, but the entire filtration of level sets. Persistence diagrams are multisets of 2-dimensional points, and thus one is faced with comparing such 2-dimensional point sets. To this end, one can use the kernel trick to implicitly map the persistence diagram into a RKHS and use the corresponding RKHS geometry in our DQF approach. The kernel we are using is the persistence scale-space kernel (PSSK)  $k_\sigma$  of Reininghaus et al. (2015). Based on this we construct the Gram matrix on which the aDQF is based, with the resulting aDQF plot shown in figure 10, which provided stronger visual evidence than the non-adaptive DQF.

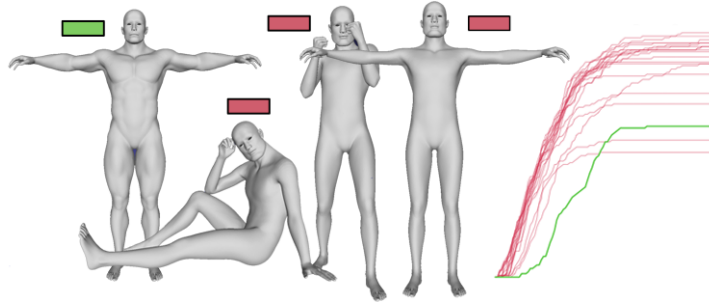


Figure 10: aDQFs  $\bar{q}_i(\delta)$  based on a kernel defined on persistence diagrams. Red lines correspond to 20 poses of one body, green line corresponds to a single pose of a different body (outlier). Tuning parameters of  $t = 500$  for the HKS and  $\sigma = 1$  for the PSSK were used.

Our second example in this subsection is considering gerrymandering. We follow the techniques of Duchin, et al. (2021) to compute a persistence diagram based on a graph representation of districting maps filtered by Republican vote percentage in the 2012 Pennsylvania Senate election. Again one can think of these persistence diagrams being constructed by first constructing a function over each potential districting map. This is accomplished by associating each districting map with a graph (vertices are the districts; edges are placed between vertices if the districts physically share a part of their boundary). Then, a function is constructed over this graph, by defining a function value at each vertex (district), which is given by the portion of Republican votes (based on counts of precincts at a given election). Then, as in our previous example, one constructs a persistence diagram for this function by again using its level set filtration. This is done for both the 2011 map invalidated by the Supreme Court for partisan gerrymandering as well as random maps generated according to the ReCom algorithm (Deford, et al. 2021). The idea is that these randomly chosen districting maps constitute a representative sample of maps, and they are being used to answer the question of whether the gerrymandered map is an anomaly.

In our analysis, the aDQFs were again computed using the kernel trick via PSSK, resulting in a visualization of the extent at which the 2011 map is anomalous, see figure 11.

## 5 Implementation

The computational complexity of the method is somewhat high, due primarily to the construction of a matrix of feature functions, as pairs of points are considered. Since we are not working with these individual functions directly but rather their averages, we propose basing these averages on only a subset of these pairwise comparisons. For a fixed number of comparisons, this allows

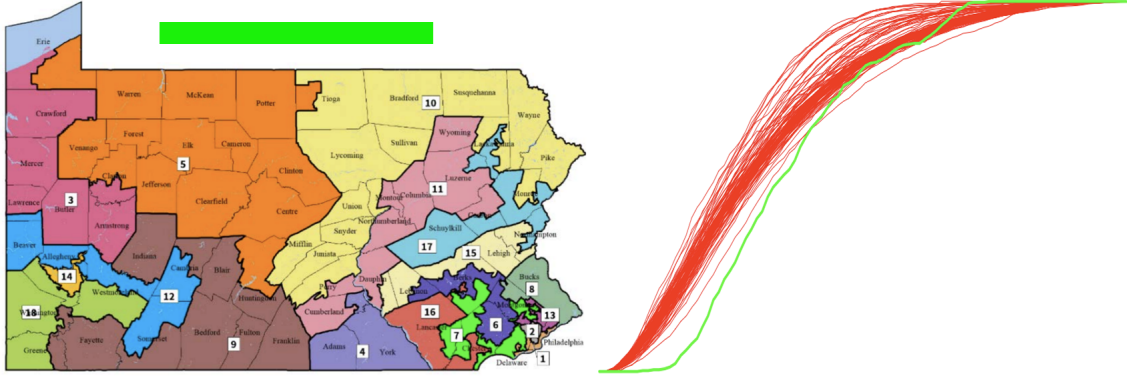


Figure 11: Normalized aDQFs  $\tilde{q}_i(\delta)$  based on a kernel defined on persistence diagrams. Red lines correspond to 99 randomly generated districting maps via ReCom, green corresponds to 2011 map (pictured, source: <https://ballotpedia.org/>) invalidated by the Supreme Court in 2018 for partisan gerrymandering.

the complexity to grow linearly in the sample size rather than quadratic. The algorithm is also embarrassingly parallel.

We propose using three visualizations of the (a)DQFs, the averaged (over a random subset)  $\bar{q}_i(\delta)$ , its normalized (by the maximal value) version,  $\tilde{q}_i(\delta)$ , and the first derivative of the normalized version  $\frac{d}{d\delta}\tilde{q}_i(\delta)$  (after a small amount of smoothing), at multiple values of  $\alpha$  (which as discussed above, does not add much computational complexity to the algorithm). The functions *dqf.outlier* and *dqf.explore*<sup>1</sup> generate and visualize these three functions as interactive plots in base-R.

For instance, the 30-dimensional simulation data demonstrates the need to consider multiple angles. For sufficiently high dimension, there is likely to exist a range of  $\delta$  such that  $\hat{q}_{ij}(\delta) = \frac{1}{n}$  for all  $i, j$ , as these cones will only include the two points  $x_i$  and  $x_j$  that define the direction. This is apparent in figure 12 at angle  $\alpha = \pi/6$ .

As a real data example, we consider the *wine* data, commonly used for illustrating classification algorithms and available at the UCI Machine Learning Repository (<https://archive.ics.uci.edu/>). The data set was subsampled by considering all 59 class 1 observations and 3 random points from other classes (observations 122, 153, and 164 from the full data set) to see if it is possible to detect these three anomalous observations. The functions above generate the plots shown in the right panel of figure 12. All three outliers differentiate themselves from the fairly homogenous aDQFs corresponding to the class 1 observations.

Rather than consider the current method as competing with existing outlier detection algorithms, we rather view the (a)DQF as complementary. It's clear from the simulation studies and real data examples that both the (a)DQF and *stray* are effective at identifying anomalous observations. Many other effective techniques exist as well. Due to the computational complexity of computing the (a)DQF (mainly with respect to sample size), identifying a suitable subset of the data to visualize via a more computationally friendly method such as *stray* for very large data sets would ease the computational burden. That is, one can compute the (a)DQF of a random subset of non-anomalous observations and any identified *interesting* observations to create a useful visualization of subsets of the data.

<sup>1</sup>available at <https://github.com/GabeChandler/AnomalyDetection>



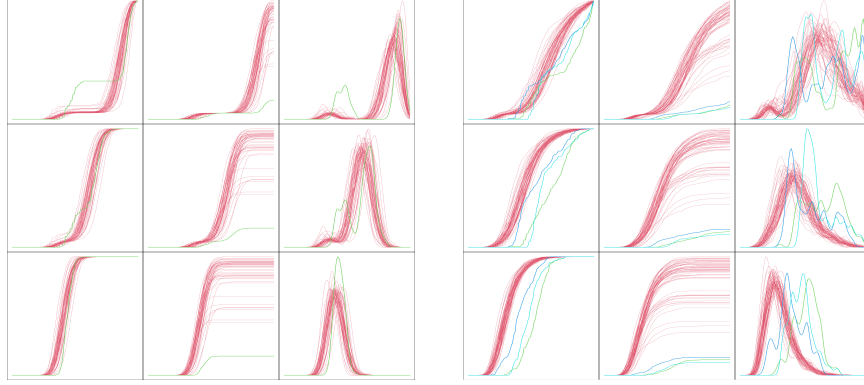


Figure 12: Visualization of (left column) normalized aDQFs  $\tilde{q}_i(\delta)$ , (center column) raw averaged aDQFs  $\bar{q}_i(\delta)$  and (right column) first derivative of normalized aDQF  $\frac{d}{d\delta}\tilde{q}_i(\delta)$  for the (left panel)  $d = 30$  simulation data and the (right panel) subsampled wine data. Outliers indicated by color. Rows correspond to different angles ( $\alpha = \pi/6, \pi/4, \pi/3$ ).

## 6 Technical proofs.

PROOF OF LEMMA 2.1. By definition of  $d_x(s)$ , we have that  $d_x(s)$  is continuous,  $d_x(x) = 0$ , and  $d_x(s)$  is non-decreasing for  $s \in [x, 1]$  and non-increasing for  $s \in [0, x]$ . Thus for each  $0 \leq t \leq 1$  there exist  $0 \leq a_x(t) \leq b_x(t) \leq 1$  with  $\{s : d_x(s) \leq t\} = [a_x(t), b_x(t)]$ . Let  $S \sim G = U(0, 1)$ . The random depth that we are considering here is  $d_x(S)$ , and its cdf is

$$D_x(t) = P(d_x(S) \leq t) = b_x(t) - a_x(t). \quad (7)$$

We further have  $D_x(TD(x)) = 1$ , and with  $\delta_x^*$  given in (4),

$$\lim_{t \nearrow TD(x)} D_x(t) = \delta_x^*. \quad (8)$$

To see (8), simply find the smallest value  $s^*$  for which  $d_x(s^*)$  attains its maximum  $TD(x)$ . Then, the limit in (8) equals  $s^*$  in case  $s^* > x$ , and  $1 - s^*$  for  $s^* < x$ . To find  $s^*$  for  $x$  with  $F(x) < \frac{1}{2}$  (i.e.  $TD(x) = F(x)$ ), note that  $d_x(s) < F(x)$  for  $s < x$ , so that  $s^* > x$ . So we simply find  $s^*$  by solving  $F(s^*) - F(x) = F(x)$  (see (1)), which gives  $s^* = F^{-1}(2F(x))$ . The case  $F(x) > \frac{1}{2}$  is similar. If  $F(x) = \frac{1}{2}$  then there is no value  $s^*$  for which  $d_x(s^*) = TD(x)$ , and in this case the limit in (8) equals 1, which immediately follows from (1). So unless  $TD(x) = \frac{1}{2}$ , i.e. unless  $x$  is the median of  $F$ , the function  $D_x(t)$  has a discontinuity at  $t = TD(x)$ .

Another needed observation is the following. Recall (see (7)) that  $D_x(t)$  equals the length of an interval (the sublevel set of  $d_x(s)$  at level  $t$ ). Given such a sublevel set  $[a, b]$  of length  $\delta < \delta_x^*$ , the values of  $d_x(s)$  at the boundaries of this interval are  $d_x(a) = F(a) - F(x)$  and  $d_x(b) = F(x) - F(b)$ , respectively. Since  $[a, b]$  is a sublevel set of  $d_x(s)$ , these values need to be equal to the corresponding level, and their sum equals  $F(b) - F(a)$ , the probability content of the interval. In other words, the level corresponding to a sublevel set of length  $\delta < \delta_x^*$  equals half of the probability content of the sublevel set. Since

$$q_x(\delta) = \inf\{t : D_x(t) \geq \delta\},$$

the above arguments now give that  $q_x(\delta)$  reaches its maximum value  $TD(x)$  at  $\delta_x^*$  given by the limit in (8). Now let  $\Delta_x$  be the set of all the lengths of the sublevel sets  $d_x(s)$ , i.e.  $\Delta_x = \{\delta \in [0, 1] : \exists t_\delta \text{ with } D_x(t_\delta) = \delta\}$ . For  $\delta \in \Delta_x$  with  $\delta < \delta_x^*$ , we have  $q_x(\delta) = t_\delta$ , and the above arguments imply that  $q_x(\delta) = t_\delta = \frac{1}{2}F(a_{x,\delta}, b_{x,\delta})$ , where  $a_{x,\delta} = a_x(t_\delta)$  and  $b_{x,\delta} = b_x(t_\delta)$ .

It remains to show (5) for values of  $\delta \in [0, 1] \setminus \Delta_x$ . They correspond to levels  $t_\delta$  at which the cdf  $D_x(t)$  is not continuous, or  $q_x(\delta)$  has a flat part. More precisely, for  $\delta \in [0, 1] \setminus \Delta_x$ , let  $\delta_u = \inf\{\gamma \in \Delta_x : D_x(t_\gamma) \geq \delta\}$  and  $\delta_\ell = \sup\{\gamma \in \Delta_x : D_x(t_\gamma) < \delta\}$ . Then,  $\delta_\ell \leq \delta \leq \delta_u$  (with at least one of the inequalities being strict). For any sequence  $\{\delta_m\} \subset \Delta_x$  with  $\delta_m \searrow \delta_u$ , the corresponding sequence  $t_{\delta_m} = \frac{1}{2}F([a_x(t_{\delta_m}), b_x(t_{\delta_m})])$  converges to  $t_\delta$ , and the intervals  $[a_x(t_{\delta_m}), b_x(t_{\delta_m})]$  converges (the endpoints converge monotonically) to an interval  $[a_{\delta_u}, b_{\delta_u}]$  with  $d_x(a_{\delta_u}) = d_x(b_{\delta_u}) = \frac{1}{2}F([a_{\delta_u}, b_{\delta_u}]) = t_\delta$ . Similarly, for  $\{\delta_{m'}\} \subset \Delta_x$  with  $\delta_{m'} \nearrow \delta_\ell$ , the corresponding sequence of intervals  $[a_x(t_{\delta_{m'}}), b_x(t_{\delta_{m'}})]$  converge to an interval  $[a_{\delta_\ell}, b_{\delta_\ell}]$  with  $[a_{\delta_u}, b_{\delta_u}] \subset [a_{\delta_\ell}, b_{\delta_\ell}]$ , and  $t_\delta = \frac{1}{2}F([a_{\delta_\ell}, b_{\delta_\ell}])$ . Geometrically, the function  $d_x(s)$  has a flat part (is constant equal to  $t_\delta$ ) on  $A_x = [a_{\delta_\ell}, b_{\delta_\ell}] \setminus [a_{\delta_u}, b_{\delta_u}]$ , where  $A_x$  has strictly positive Lebesgue measure, but  $F(A_x) = 0$ . In particular,  $x$  is the median for any interval  $[a, b]$  with  $[a_{\delta_u}, b_{\delta_u}] \subset [a, b] \subset [a_{\delta_\ell}, b_{\delta_\ell}]$ . So, we have  $q_x(\delta) = \frac{1}{2}F[a_{x,\delta_u}, b_{x,\delta_u}] = \frac{1}{2}F[a_{x,\delta_\ell}, b_{x,\delta_\ell}] = \frac{1}{2}F([a, a + \delta])$ . This completes the proof of (5).

To see the last assertion of the lemma, observe that

$$\lim_{t \searrow 0} D_x(t) = l_x. \quad (9)$$

In particular, this implies that for  $x \notin \text{supp}(F)$ ,  $D_x(t)$  has a discontinuity at  $t = 0$ , and thus, for such values of  $x$ , the DQF  $q_x(\delta)$  is constant equal to zero for  $\delta \in [0, l_x]$ .

□

**Proof of Lemma 2.2:** By definition of  $t_{x,y}^\pm$ , we have  $F(A_{x,y}(s)) = 0$  for  $s \in (m_{x,y} - t_{x,y}^-u, m_{x,y} + t_{x,y}^+u) \subseteq [a_{x,y}, b_{x,y}]$ . From this we have that  $d_{x,y}(s) = \min(F(A_{x,y}(s)), B_{x,y}(s)) = 0$ . The  $G_{x,y}$ -measure of this set equals  $l_{x,y} = \frac{t_{x,y}^+ + t_{x,y}^-}{\|b_{x,y} - a_{x,y}\|}$ . It follows that  $q_{x,y}(\delta) = 0$  for  $\delta \in [0, l_{x,y}]$ , and thus have  $q_{x,y}(\delta) = 0$  for all  $\delta \in [0, \inf_y l_{x,y}]$ . This implies that  $\bar{q}_x(\delta) = 0$  for all  $\delta \in [0, \inf_y l_{x,y}]$ .

□

## 7 References

- Aggarwal, C.C. (2013): Outlier Analysis. Springer, New York.
- Burridge, P., and Taylor, R. (2006): Additive Outlier Detection Via Extreme-Value Theory. *J. Time Ser. Anal.* **27**. 685-701.
- Chandler, G. and Polonik, W. (2021): Multiscale geometric feature extraction for high-dimensional and non-Euclidean data with applications. *Ann. Statist.* **49**, 988-1010.
- Chazal, F. and Michel, B. (2021): An introduction to topological data analysis: fundamental and practical aspects for data scientists. *Front. Artif. Intell.*, 4.
- DeFord, D., Duchin, M. and Solomon, J. (2021): Recombination: A Family of Markov Chains for Redistricting. *Harvard Data Sci. Rev.*
- Duchin, M., and Needham, T. and Weighill, T. (2021): The (homological) persistence of gerrymandering. *Found. Data Sci.* 10.3934/fods.2021007.
- Einmahl, J. H. J., Gantner, M., and Sawitzki, G. (2010a): The Shorth Plot. *J. Comput. Graphical Stat.*, **19**(1), pp. 62-73.
- Einmahl, J. H. J., Gantner, M., and Sawitzki, G. (2010b): Asymptotics of the shorth plot. *J. Stat. Plann. Inference*, **140**, pp. 3003-3012.



- Fefferman, C., Mitter, S., and Narayanan, H. (2016): Testing the manifold hypothesis. *J. Am. Math. Soc.* **29**, 983–1049.
- Fisher, M. A., Friedman, J. H. and Tukey, J. W. (1974): PRIM-9, an interactive multidimensional data display and analysis system. *Proceedings of the Pacific ACM Regional Conference*. [Also in *The Collected Works of John W. Tukey V* (1988) pp. 307–327.]
- Friedman, J.H. and Stuetzle, W. (2002): John W. Tukey’s work on interactive graphics. *Ann. Statist.*, **30**, pp. 1629–1639.
- Hawkins, D. M. (1980): Identification of Outliers. Chapman and Hall, London – New York.
- Hyndman, R. J., (1996): Computing and graphing highest density regions. *Am. Stat.*, **50**, 120–126.
- Hodge, V.J. and Austin, J. (2004): A survey of outlier detection methodologies. *Artif. Intell. Rev.*, **22** (2). pp. 85–126.
- Lientz, B. P. (1974): Results on nonparametric modal intervals, *SIAM J. Appl. Math*, **19**, pp. 356–366.
- Minnotte, M. and Scott, D. (1997): The Mode Tree: A Tool for Visualization of Nonparametric Density Features. *J. Comput. Graphical Stat.* **2**.
- Olson, C.C., Judd, K.P., Nichols, J.M. (2018): Manifold learning techniques for unsupervised anomaly detection, *Expert Syst. Appl.*, **91**, 374–385.
- Reininghaus, J., Huber, S., Bauer, U. and Kwitt, R. (2015): A stable multi-scale kernel for topological machine learning. *IEEE Conference on Computer Vision and Pattern Recognition (CVPR)*, pp. 4741–4748.
- Rényi, A. and Sulanke, R. (1963): Über die konvexe Hülle von  $n$  zufällig gewählten Punkten I. *Z. Wahrsch. Verw. Gebiete*, **2**:75–84.
- Ruff, L., Kauffmann, J., Vandermeulen, R., Montavon, G., Samek, W., Kloft, M., Dietterich, T., and Müller, K. (2021): A Unifying Review of Deep and Shallow Anomaly Detection. *Proceedings of the IEEE*. 1–40.
- Sun, J., Ovsjanikov, M. and Guibas, L. (2009): A concise and probably informative multi-scale signature based on heat diffusion. *Eurographics Symposium of Geometry Processing*, **28**.
- Sawitzki, G. (1994): Diagnostic plots for one-dimensional data. In: Ostermann, R., Dirschedl, P. (Eds.), *Computational Statistics, 25th Conference on Statistical Computing at Schloss Reisensburg*. Physica-Verlag, Springer, Heidelberg, pp. 237–258.
- Talagala, P.D., Hyndman, R.J. and Smith-Miles, K. (2021): Anomaly Detection in High-Dimensional Data, *J. Comput. Graphical Stat.*, DOI: 10.1080/10618600.2020.1807997
- Tenenbaum JB, de Silva V., and Langford JC. (2000): A global geometric framework for nonlinear dimensionality reduction. *Science*. **290**(5500) pp. 2319–23.
- Tukey, J. W. (1975): Mathematics and the picturing of data. *Proceedings of the International Congress of Mathematicians. 1975*. pp.523–531.
- Wasserman, L. (2018): Topological data analysis. *Annu. Rev. Stat. Appl.*, **5**, pp. 1501–532.
- Wilkinson, L. (2017), Visualizing big data outliers through distributed aggregation. *IEEE Trans. Visual Comput. Graphics* **24**(1), pp. 256–266.